Maximum-entropy meshfree method for nonlinear static analysis of planar reinforced concrete structures

Giuseppe Quaranta[1], Sashi K. Kunnath, Natarajan Sukumar
Department of Civil and Environmental Engineering, University of California, Davis, CA 95616, United States

Abstract

A meshfree method for nonlinear analysis of two-dimensional reinforced concrete structures subjected to monotonic static loading is presented. The concrete model is implemented in the context of the smeared rotating crack approach. The stress-strain relationship for steel bars accounts for the surrounding concrete bonded to the bar (tension stiffening effect). The principle of virtual work (variational form) is used to setup the nonlinear system of equations. Maximum-entropy basis functions are used to discretize the two-dimensional domain and background cells are adopted to facilitate the numerical integration. The generalized displacement control method is implemented to solve the nonlinear system of equations and to obtain the softened structural response beyond the maximum load capacity. The proposed meshfree methodology is used to study the nonlinear behavior of reinforced concrete shear walls. Comparisons with experimental data and finite element analysis indicate that the proposed maximum-entropy meshfree method is a viable approach for nonlinear simulations of planar RC structures.

Keywords: generalized displacement control method, meshfree method, maximum-entropy basis functions, nonlinear static analysis, reinforced concrete, shear wall.

1. Introduction

The response of reinforced concrete (RC) structures is typically solved within the framework of the finite element (FE) method, thus requiring a priori discretization of the domain through the definition of a mesh. Because of the intrinsic (geometrical and/or material) nonlinearities in most problems of practical interest dealing with RC structures, significant effort has gone into improving existing models for simulating RC behavior as well as enhancing the accuracy and reliability of solutions obtained by FE methods. On the contrary, very little effort has gone into exploring new numerical methods for the analysis of RC structures that may have the potential to establish new and effective paradigms in modern structural analysis.

[1] Corresponding author. E-mail: gquaranta@ucdavis.edu. Tel.: +1 (530) 754 6416

To this end, meshfree (or meshless or element-free) methods are gaining popularity as effective tools for advanced numerical analyses. To date, meshfree methods are routinely used for very specialized applications in computational and solid mechanics. In contrast, less effort has been devoted toward applying meshfree methods in common structural engineering problems.

In order to explore the viability of meshfree-based computational tools in the field of structural engineering, Yaw and co-workers [1] presented a blended FE and meshfree Galerkin approximation scheme to study the inelastic response of plane steel frames with J_2 plasticity. The same authors also proposed a meshfree co-rotational formulation for two-dimensional continua in the presence of small strains with elastic and elasto-plastic material behavior [2]. Current trends in meshfree applications on the analysis of RC structures essentially exploit their natural ability in modeling static or dynamic fracture phenomena in brittle materials. For instance, Rabczuk and co-workers [3] presented a geometrically non-linear three-dimensional crack method in which the element free Galerkin (EFG) method was used for concrete modeling, a cohesive zone model was adopted after crack initiation and the reinforcement (modeled by truss or beam elements) is connected by a bond model to the concrete. A coupled FE-meshfree method was also presented by Rabczuk and Eibl [4] for the analysis of pre-stressed concrete beams.

In this paper, a meshfree method is developed for nonlinear analysis of two-dimensional RC structures subjected to static monotonic loading. To this end, concrete modeling issues are first addressed (Section 2), and then the adopted model for uncracked, partially cracked and fully cracked concrete under plane stress condition is presented. This is followed by the description of the steel constitutive model (Section 3). In Section 4, the meshfree-based nonlinear system of equations is derived from the variational weak form, and maximum-entropy basis functions are used to discretize the domain. Subsequently, the adopted numerical strategy to solve for the resulting nonlinear system of equations is discussed. In Section 5, the validity of the method is demonstrated through comparisons with experimental data and FE analysis of shear walls subjected to monotonic static loading. Finally, some closing remarks are made in Section 6 on the future development of the present work.

2. Concrete modeling

2.1. Modeling of cracked concrete

The FE analysis of RC structures needs an appropriate approach for modeling cracked concrete, e.g. smeared crack [5] and discrete crack approaches [6]. Smeared crack based models tend to be more popular than the discrete crack models due to their improved ability to account for multi-axial stress

states in concrete, and also because they are more convenient from a programming point-of-view. A smeared crack approach is intended to preserve the continuity of the displacement field over the domain of influence of the cracked node by representing many (fictitious) finely spaced cracks parallel to the dominant discrete (real) crack. With this continuum approach, the local displacement discontinuities at cracks are artificially smeared over the tributary area, and the behavior of cracked RC is represented by average stress-strain relations for both concrete and steel.

Although meshfree methods provide an effective theoretical background to deal with discrete representation of cracks, the use of a smeared crack approach aims at supporting future blended FE-meshfree approaches for nonlinear analysis of RC structures. In fact, as long as standard FE methods have strong limitations in discrete crack modeling, a smeared approach can be used in both FE and meshfree domains, thus providing a unique framework for concrete crack modeling.

A pure smeared rotating crack model is hence adopted in this study. Several studies demonstrate that smeared crack models for RC modeling are physically consistent and show good agreement with experimental data. On the other hand, it is well known that FE analyses using work-softening brittle materials within smeared crack models show significant mesh-sensitivity problems. Our preliminary analyses of unreinforced concrete structures with smeared crack models revealed that a similar issue also occurs in meshfree methods. In particular, it was found that the load capacity decreases moderately as the nodal spacing reduces whereas the slope of the softening branch increases considerably, which is consistent with FE analyses [7]. To alleviate the above issues, averaging concept in tension stiffening [8] and the crack band model [9,10] are implemented. The width h of the crack band is assumed to be equal to the square root of the area of the domain of influence for rectangular shapes or to its diameter in the case of circular shapes. The stress-locking problem in the vicinity of dominant cracks that is attributed to the smeared crack model can be reduced by employing the smeared rotating crack model, which is more popular than the smeared fixed crack model [5,8,9].

2.2. Constitutive matrix for concrete

The x-y coordinate system represents the geometrical coordinates at the integration point. On the other hand, the 1-2 coordinate system represents the mechanical (local) coordinates at the integration point and coincides with the principal stress directions. Plane stress condition is assumed and the angle between the x-axis and the 1-axis is denoted as θ. It has been experimentally observed that directions of principal strains in the concrete deviate somewhat from the directions of principal stress, Vecchio and Collins [11] concluded that it is a reasonable simplification to assume that the principal strain axes and the principal stress axes for the concrete coincide. Let $\boldsymbol{\varepsilon} = \{\varepsilon_x \ \varepsilon_y$

$\gamma_{xy}\}^T$ be the strain in the geometrical system of reference. Therefore, the following transformation holds

$$\boldsymbol{\varepsilon}_{(12)} = \mathbf{T}_c(\theta)\boldsymbol{\varepsilon} \tag{1}$$

in which $\boldsymbol{\varepsilon}_{(12)} = \{\varepsilon_1\ \varepsilon_2\ \gamma_{12}\}^T$ is the strain vector in the local system of reference and $\mathbf{T}_c(\theta)$ is the strain transformation matrix. For the implementation procedure in this study, a tangent material stiffness matrix is considered [8,12]. The relation between incremental stresses $d\boldsymbol{\sigma}_{(12)}=\{d\sigma_1\ d\sigma_2\ d\tau_{12}\}^T$ and incremental strains $d\boldsymbol{\varepsilon}_{(12)}=\{d\varepsilon_1\ d\varepsilon_2\ d\gamma_{12}\}^T$ in the 1-2 coordinate system of reference is

$$d\boldsymbol{\sigma}_{(12)} = \mathbf{D}_c d\boldsymbol{\varepsilon}_{(12)} \tag{2}$$

Referring to the principal axis 1-2, it is assumed that the tangent constitutive matrix $\mathbf{D}_c$ for concrete before cracking takes the form [13]

$$\mathbf{D}_c = \frac{1}{1-\nu^2}\begin{bmatrix} E_{c1} & \nu\sqrt{E_{c1}E_{c2}} & 0 \\ \nu\sqrt{E_{c1}E_{c2}} & E_{c2} & 0 \\ 0 & 0 & (1-\nu^2)G_c \end{bmatrix} \tag{3}$$

in which E_{c1} and E_{c2} are the concrete tangent moduli, G_c is the shear modulus and ν is the Poisson ratio. Once concrete cracking is initiated either in 1-direction or 2-diretion, the tangent constitutive matrix given by Eq. (3) is replaced with the following

$$\mathbf{D}_c = \frac{1}{1-\nu^2}\begin{bmatrix} E_{c1} & 0 & 0 \\ 0 & E_{c2} & 0 \\ 0 & 0 & G_c \end{bmatrix} \tag{4}$$

as in Ref. [12]. As the loading progresses, a set of smeared cracks fully opens into the concrete. In this case, Eq. (4) is replaced with the following [14]

$$\mathbf{D}_c = \begin{bmatrix} 0 & 0 & 0 \\ 0 & E_{c2} & 0 \\ 0 & 0 & \mu G_c \end{bmatrix} \tag{5}$$

where E_{c2} is the tangent modulus of concrete parallel to the crack direction and μ is the shear retention factor introduced to provide for shear friction across fully opened cracks. Various forms of this shear factor have been proposed until now. However, numerous analytical results have demonstrated that the particular value chosen for μ (between 0 and 1) does not appear to be critical, but values greater than zero are suggested to prevent numerical instabilities [9,14].

Upon further loading, a second set of smeared cracks can form in the direction normal to the first set of smeared cracks. In this case, the constitutive matrix is:

$$\mathbf{D}_c = \begin{bmatrix} 0 & 0 & 0 \\ 0 & 0 & 0 \\ 0 & 0 & \mu G_c \end{bmatrix} \tag{6}$$

Moreover, when the concrete strain exceeds the ultimate concrete strain in compression in one or two directions, concrete failure by crushing occurs. In this case, the element is assumed to lose its strength completely and is not able to carry any more stress. Because of material nonlinearities, all quantities in the above constitutive matrices usually vary as functions of the stress and strain fields.

2.3. Concrete strength due to confinement effect

Let f_c be the uniaxial concrete compressive strength and ε_c the concrete strain at f_c. For unconfined concrete, $f_c = f_c'$ and $\varepsilon_c = \varepsilon_c'$, in which f_c' and ε_c' are the uniaxial compressive strength and the corresponding strain for concrete without (or with modest or inefficient) confinement reinforcement. It is well known that the uniaxial concrete compressive strength and the corresponding strain increase if appropriate confinement reinforcement is provided. To account for this phenomenon, the model proposed by Hoshikuma and co-workers [15] is considered

$$\begin{aligned} f_c &= f_c' + 3.8 c_1 \rho_z f_{y,z} \\ \varepsilon_c &= 0.002 + 0.033 c_2 \frac{\rho_z f_{y,z}}{f_c'} \end{aligned} \tag{7}$$

where $f_{y,z}$ is the yielding stress of the confinement reinforcement and ρ_z the confinement reinforcement ratio. Parameters c_1 and c_2 depend on the shape of the confined section. For square sections, Hoshikuma and co-workers [15] suggested c_1 = 0.2 and c_2 = 0.4. It is assumed that confinement has no effect on concrete tensile strength.

2.4. Concrete strength under biaxial stress

It is well known that the concrete strength significantly depends on the current stress-strain state. It is assumed that both the uniaxial concrete compressive strength and the corresponding strain depend on the current stress- and/or strain-state at the considered integration point, i.e.,

$$f_{cp} = \alpha f_c \tag{8}$$

$$\varepsilon_{cp} = \alpha \varepsilon_c \tag{9}$$

where α is the scaling factor depending on stresses or strains in the assumed principal directions.

The strength enhancement factor for concrete subjected to compression in the 2-direction, arising from the compressive stress σ_1 acting in the 1-direction, is given by [16]:

$$\alpha = 1 + 0.92\left(-\frac{\sigma_1}{f_c}\right) - 0.76\left(-\frac{\sigma_1}{f_c}\right)^2 . \tag{10}$$

Similarly, the strength enhancement factor for concrete subjected to compression in the 1-direction, arising from the compressive stress σ_2 acting in the 2-direction, is given by

$$\alpha = 1 + 0.92\left(-\frac{\sigma_2}{f_c}\right) - 0.76\left(-\frac{\sigma_2}{f_c}\right)^2 \tag{11}$$

In the tension-compression state, the major principal stress is tensile and it reduces the compressive strength in the minor principal direction. In this case, the scaling factor adopted in this study takes the form

$$\alpha = \frac{1}{0.8 + 0.34\dfrac{\varepsilon_+}{\varepsilon_c}} \le 1 \tag{12}$$

where ε_+ is the principal tensile strain. It is assumed that the concrete tensile strength does not depend on the stress-strain state.

2.5. Relationship between biaxial strains and uniaxial strains

The uniaxial strains $\overline{\boldsymbol{\varepsilon}}_{(12)} = \{\overline{\varepsilon}_1 \quad \overline{\varepsilon}_2 \quad \overline{\gamma}_{12}\}^T$ are obtained from the biaxial strains as follows [5,8]:

$$\overline{\boldsymbol{\varepsilon}}_{(12)} = \mathbf{V}\boldsymbol{\varepsilon}_{(12)} \tag{13}$$

The adopted projection matrix $\mathbf{V}$ is

$$\mathbf{V} = \begin{bmatrix} \dfrac{1}{1-\nu_{12}\nu_{21}} & \dfrac{\nu_{12}}{1-\nu_{12}\nu_{21}} & 0 \\ \dfrac{\nu_{21}}{1-\nu_{12}\nu_{21}} & \dfrac{1}{1-\nu_{12}\nu_{21}} & 0 \\ 0 & 0 & 1 \end{bmatrix} \tag{14}$$

A lack of agreement exists on the numerical values to be used for ν_{12} and ν_{21}. He and co-workers [5] considered $\nu_{12} = \nu_{21} = \nu$, as is common in most of the existing literature. On the contrary, Zhu and Hsu [17] experimentally observed that the Poisson effect is characterized by the Poisson ratio for concrete before cracking whereas ν_{12} and ν_{21} are different from ν when concrete cracks, and

introduced the Zhu/Hsu ratios to replace it. All the above cited studies, however, claim that the final comparison with experimental data is satisfactory. Therefore, it seems that more experimental investigations are needed to resolve this issue. Following a conventional approach, in this study it is assumed that $\nu_{12} = \nu_{21} = \nu$.

As the current strength of concrete is calculated according to the biaxial stress state, the uniaxial stress-strain relationship reflects the biaxial stress state. Therefore, once the uniaxial strains are obtained and the concrete compressive strength is modified accounting for the biaxial stress state, the tangent modulus E_{c1} or E_{c2} can now be obtained by differentiating the uniaxial constitutive stress-strain relationship for concrete $\sigma_c\left(\bar{\varepsilon}_c\right)$ with respect to $\bar{\varepsilon}_c = \bar{\varepsilon}_1$ or $\bar{\varepsilon}_c = \bar{\varepsilon}_2$, respectively.

2.6. Stress-strain relationship for concrete in tension

The response of concrete in tension is usually regarded as linear until the tension strength f_{ct} has been reached, and is described by a Rankine-type principle stress criterion. At strain ε_{ct}, crack initiation and localization of a narrow process zone occurs. Subsequently, a softening behavior starts and it is usually modeled as a straight line, a piecewise linear branch, or a descending-exponential curve. In this study, the stress-strain relation for concrete in tension is based on the model proposed in Ref. [18]

$$\sigma_c\left(\bar{\varepsilon}_c\right) = \begin{cases} E_{ct0}\bar{\varepsilon}_c & if\ 0 \le \bar{\varepsilon}_c \le \varepsilon_{ct} \\ f_{ct} e^{\frac{\varepsilon_{ct}-\bar{\varepsilon}_c}{\varphi}} & if \quad \bar{\varepsilon}_c > \varepsilon_{ct} \end{cases} \tag{15}$$

which is shown in Fig. 1. In Eq. (15), φ is a (positive) shape parameter and E_{ct0} is the initial Young's modulus for concrete in tension. To reduce the lack of objectivity in the smeared crack model, the crack band theory by Bažant and Oh [10] is often adopted for the purpose of modeling tension in concrete [9,18,19]. Given G_f, the mode-*I* fracture energy of concrete, if the following condition is satisfied

$$h < \frac{G_f E_{ct0}}{f_{ct}^2}, \tag{16}$$

then the shape parameter φ is

$$\varphi = \frac{G_f}{h f_{ct}} - \frac{1}{2}\varepsilon_{ct} \tag{17}$$

If Eq. (16) is not fulfilled, then Bažant and Oh [10] proposed to modify the concrete strength in tension as follows

$$f_{ct} = \sqrt{\frac{2G_f E_{ct0}}{h}} \tag{18}$$

along with a vertical post-peak stress drop of the stress-strain relationship for concrete in tension. Since a tangent-based implementation is used in this study, a vertical post-peak stress drop may lead to numerical problems. Therefore, an exponential post-peak softening response is still adopted as in Eq. (15) and the concrete strength in tension given by Eq. (18). In doing so, the shape parameter φ and the ultimate strain of the concrete in tension ε_{ctu} are now pure material parameters, and their numerical values should be quite small in order to approximate a vertical stress drop without causing numerical instabilities.

Finally, the mode-*I* fracture energy of concrete G_f is calculated as specified in the CEB-FIP model code [20]

$$G_f\,[\mathrm{N/mm}] = \alpha_f \left(\frac{f_c'[\mathrm{MPa}]}{10} \right)^{0.7} \tag{19}$$

with $\alpha_f = 10^{-3}\left(1.25 d_{\max}\,[\mathrm{mm}] + 10\right)$, where $d_{\max}$ is the maximum aggregate size in concrete. Because of the lack of reliable experimentally-calibrated models, it is assumed that the fracture energy of concrete does not depend on confinement effect or biaxial stress states.

2.7. Stress-strain relationship for concrete in compression

The uniaxial strain-stress relationship proposed by Popovics [21] is used in this study for concrete

$$\sigma_c\left(\overline{\varepsilon}_c\right) = -\frac{\beta}{\beta - 1 + \left(\dfrac{\left|\overline{\varepsilon}_c\right|}{\varepsilon_{cp}} \right)^{\beta}} \frac{\left|\overline{\varepsilon}_c\right|}{\varepsilon_{cp}} f_{cp} \tag{20}$$

where β > 1 is a shape factor (see Fig. 1).

The softening branch for confined concrete is modeled as proposed in Ref. [15]. In doing so, the post-peak Popovics' model is replaced with a straight line having a slope:

$$E_c = 11.2 \frac{\left(f_c'\right)^2}{\rho_z f_{y,z}}. \tag{21}$$

The model for confined concrete is illustrated in Fig. 1. Concrete failure by crushing occurs once the ultimate strain of concrete in compression is achieved..

2.8. Shear modulus for concrete

Darwin and Pecknold [13] provided a rational tangent shear modulus to be used in Eq. (3) in such a way that the results are independent with respect to axis rotation. The pre-cracking shear modulus for concrete in this case is

$$G_c = \frac{1}{4\left(1-\nu^2\right)}\left(E_{c1} + E_{c2} - 2\nu\sqrt{E_{c1}E_{c2}}\right) \tag{22}$$

Several analytical, semi-analytical and empirical formulations have been proposed for the post-cracking tangent shear modulus of concrete. In this study, the post-cracking value of concrete G_c is calculated as proposed in Ref. [22]

$$G_c = \frac{\sigma_1 - \sigma_2}{2\left(\varepsilon_1 - \varepsilon_2\right)} \tag{23}$$

2.9. Poisson ratio

The Poisson ratio ν for concrete typically ranges between 0.15 and 0.22, but it has been experimentally observed that the Poisson ratio also depends on the current strain and stress states. A value for the Poisson ratio about 0.20 has been shown to be quite satisfactory for monotonic loading in tension-tension and compression-compression [13]. Because of the lack of well-settled experimental evidence, a constant Poisson ratio is assumed in this study.

2.10. Unloading-reloading scheme for concrete

Unloading-reloading can locally occur in concrete even under monotonic loading. It may be due to numerical issues (during iterations to achieve equilibrium) which depend on the smeared rotating crack model. Furthermore, a realistic RC structure has the ability to redistribute stress after a crack opens, which often leads to unloading in the concrete. To this end, the simplified unloading-reloading scheme adopted by He and co-workers [23] is assumed in this study to deal with RC structures subjected to monotonic loading (see Fig. 1). This simple unloading-reloading scheme provides satisfactory results for cyclically loaded RC structures with typical steel reinforcing ratios [5]. On the contrary, it is observed a significant difference for low steel reinforcing ratios. Therefore, this unloading-reloading scheme is a reasonable simplification for monotonic loadings only, because the accuracy at the structural level is not affected.

3. Modeling of steel reinforcement

3.1. Constitutive matrix for reinforcement

Longitudinal reinforcing steel bars are treated as an equivalent uniaxial layered material placed at the depth of the centerline of the bars and smeared over the region of bar effect [8,14,24,25]. As many layers are used as there are layers of bars in the cross section, each with its uniaxial properties oriented along the axis of the bars. The tangent constitutive matrix for the *k*th steel reinforcement layer is

$$\mathbf{D}_{sk} = \begin{bmatrix} \rho_{sk} E_{sk} & 0 & 0 \\ 0 & 0 & 0 \\ 0 & 0 & 0 \end{bmatrix} \tag{24}$$

in which ρ_{sk} is the reinforcement ratio and E_{sk} the tangent modulus for the *k*th steel reinforcement layer, both varying as function of the current strain state. A perfect bond between the concrete and the reinforcement is assumed. Steel bars were also modeled as smeared reinforcement with perfect bond by Bao and Kunnath [25] for post-peak FE-based analysis of two-dimensional RC structures under monotonic loadings. Since the bond degradation of reinforcing bars is one of the most important issues in assessing the seismic performance of RC structures, the bond-slip between the concrete matrix and the reinforcement needs to be modeled appropriately when considering cyclic loadings.

For each reinforcement layer, the uniaxial strains of steel $\overline{\boldsymbol{\varepsilon}}_{sk}$ are calculated from the uniaxial strains of concrete $\overline{\boldsymbol{\varepsilon}}_{(12)}$ in Eq. (13) as follows:

$$\overline{\boldsymbol{\varepsilon}}_{sk} = \mathbf{T}_s\left(\theta, \theta_{sk}\right) \overline{\boldsymbol{\varepsilon}}_{(12)} \tag{25}$$

where $\mathbf{T}_s(\theta,\theta_{sk})$ the strain transformation matrix and θ_{sk} is the angle between the *x*-axis and the centerline of the bars belonging to the *k*th reinforcement layer. Therefore, the tangent modulus E_{sk} can be now obtained by differentiating the uniaxial constitutive stress-strain relation for steel $\sigma_s\left(\overline{\varepsilon}_s\right)$ with respect to $\overline{\varepsilon}_s = \overline{\varepsilon}_{sk}$. The strain $\overline{\varepsilon}_{sk}$ will be the first element of the vector $\overline{\boldsymbol{\varepsilon}}_{sk}$ calculated in Eq. (25).

3.2. Stress-strain relationship for reinforcing steel

A stress-strain relationship for steel bars embedded in concrete is somewhat different from that of a bare steel bar because the surrounding concrete bonded to the bar causes tension-stiffening effect. As a consequence, the smeared stress-strain relationship of steel bars embedded in concrete must be

obtained by averaging the stresses and strains between two cracks. In this study, the envelope stress-strain relation adopted by Mansour and co-workers [26] is assumed

$$\sigma_s\left(\overline{\varepsilon}_s\right)=\begin{cases} E_{s0}\overline{\varepsilon}_s & if \quad \left|\overline{\varepsilon}_s\right|\le \varepsilon_n \\ f_y\left(\left(0.91-2B\right)+\left(0.02+0.25B\dfrac{\overline{\varepsilon}_s}{\varepsilon_y}\right)\right) & if \quad \left|\overline{\varepsilon}_s\right|> \varepsilon_n \end{cases} \tag{26}$$

$$\varepsilon_n=\varepsilon_y\left(0.93-2B\right) \tag{27}$$

$$B=\left(f_{ct}/f_y\right)^{1.5}\Big/\max\{\rho_s,0.25\%\} \tag{28}$$

where E_{s0} is the initial (elastic) modulus of steel, ρ_s the reinforcement ratio, f_y the yielding stress and ε_y the yielding strain. The model is illustrated in Fig. 2. All these quantities are referred to the corresponding kth reinforcement layer. The ultimate strength of reinforcing steel is denoted as f_{su}.

A simple bi-linear elasto-plastic hysteretic model with kinematic hardening is adopted to model the unloading-reloading behavior of reinforcing steel bars, see Fig. 2. This simplified model is routinely used in modeling reinforcing bars in RC structures, such as in Kabeyasawa and Milev [12] for modeling RC shear walls subjected to cyclic loadings. Although more accurate models were recently proposed to describe the unloading-reloading behavior of reinforcing steel bars, this simplified scheme provides satisfactory results at the structural level under the assumption of monotonic loading.

4. Variational formulation and discrete equations

4.1. Equilibrium equation

The variational weak form is formulated in the global *x-y* coordinate system. The displacement approximation $\mathbf{u}^h$ is of the form

$$\mathbf{u}^h=\mathbf{\Phi}^T\mathbf{d} \tag{29}$$

in which $\mathbf{\Phi}$ is the matrix that consists of meshfree basis functions and $\mathbf{d}$ is the vector of nodal parameters. The strain-displacement relation is

$$\boldsymbol{\varepsilon}=\mathbf{B}\mathbf{d} \tag{30}$$

where $\mathbf{B}$ is the strain–displacement matrix. The weak form (principle of virtual work) for problems in structural mechanics leads to the equilibrium equations:

$${}^{ext}\mathbf{f}-{}^{int}\mathbf{f}=\mathbf{0} \tag{31}$$

where ${}^{ext}\mathbf{f}$ is the vector of external loads

$${}^{ext}\mathbf{f} = \int_{\Omega} \mathbf{\Phi}^T \mathbf{b} \mathrm{d}\Omega + \int_{\Gamma_t} \mathbf{\Phi}^T \mathbf{t} \mathrm{d}\Gamma \tag{32}$$

and ${}^{int}\mathbf{f}$ the vector of internal forces

$${}^{int}\mathbf{f} = \int_{\Omega} \mathbf{B}^T \boldsymbol{\sigma} \mathrm{d}\Omega \tag{33}$$

In Eq. (32) and Eq. (33), $\mathbf{b}$ is the body force vector acting on Ω, $\mathbf{t}$ the prescribed traction on the natural boundary Γ_t and $\boldsymbol{\sigma} = \{\sigma_x \ \sigma_y \ \sigma_{xy}\}^T$ the stress vector. Generally Eq. (31) is a nonlinear system of equations, because the unknown stress field is a nonlinear function of the strain field. As a consequence, an appropriate incremental-iterative numerical procedure has to be adopted to solve for the unknown displacement field. The incremental-iterative form of the equilibrium equation is

$$\mathbf{K}^i_{(j-1)} \Delta \mathbf{d}^i_j = \Delta \lambda^i_j \, {}^{ext}\hat{\mathbf{f}} + \mathbf{r}^i_{(j-1)} \tag{34}$$

in which i denotes the current load increment step, j is the current iteration number, $\Delta \mathbf{d}^i_j$ is the increment of the vector of nodal parameters, ${}^{ext}\hat{\mathbf{f}}$ is the reference external load vector, $\Delta \lambda^i_j$ is the load increment parameter (proportional static loading), $\mathbf{r}^i_{(j-1)}$ is the unbalanced force vector

$$\mathbf{r}^i_{(j-1)} = {}^{ext}\mathbf{f}^i_{(j-1)} - {}^{int}\mathbf{f}^i_{(j-1)} \tag{35}$$

In Eq. (34), $\mathbf{K}^i_{(j-1)}$ is the tangent stiffness matrix formed at the beginning of the jth iteration and it is based on the known information carried out at the $(j-1)$th iteration. It is obtained as an assembly process of the 2×2 nodal tangent stiffness matrices $\mathbf{K}_{IJ}(\mathbf{d}^i_{(j-1)})$

$$\mathbf{K}^i_{(j-1)} = \mathop{\mathrm{A}}_{I,J}^{n} \mathbf{K}_{IJ}\left(\mathbf{d}^i_{(j-1)}\right) = \mathop{\mathrm{A}}_{I,J}^{n} \left(\int_{\Omega} \mathbf{B}_I^T \mathbf{C}\left(\mathbf{d}^i_{(j-1)}\right) \mathbf{B}_J \mathrm{d}\Omega \right) \tag{36}$$

where $I, J = 1,\ldots,n$ denote two nodes within Ω and $\mathbf{C}(\mathbf{d}^i_{(j-1)})$ is the tangent constitutive in the global system of reference x-y. The integral in Eq. (36) vanishes if I and J do not belong to the same local support domain. Once $\mathbf{D}_c(\mathbf{d}^i_{(j-1)})$ and $\mathbf{D}_{sk}(\mathbf{d}^i_{(j-1)})$ are calculated as in Eqs. (3)-(6) and in Eq. (24), they are rotated into the x-y coordinate system, thus obtaining $\mathbf{C}_c(\mathbf{d}^i_{(j-1)})$ and $\mathbf{C}_{sk}(\mathbf{d}^i_{(j-1)})$, respectively. Having done so, the tangent constitutive matrix $\mathbf{C}(\mathbf{d}^i_{(j-1)})$ in Eq. (36) is

$$\mathbf{C}\left(\mathbf{d}^i_{(j-1)}\right) = \mathbf{C}_c\left(\mathbf{d}^i_{(j-1)}\right) + \sum_{k}^{n_k} \mathbf{C}_{sk}\left(\mathbf{d}^i_{(j-1)}\right) \tag{37}$$

where n_k is the total number of reinforcing layers.

Numerical integration based on background cells is used to evaluate the integrals in Eq. (32), Eq. (33) and Eq. (36). For example, the 2×2 nodal tangent stiffness matrices $\mathbf{K}_{IJ}(\mathbf{d}^i_{(j-1)})$ in Eq. (36) is evaluated as follows

$$\mathbf{K}_{IJ}\left(\mathbf{d}^i_{(j-1)}\right)=\sum_{c}^{n_c}\sum_{g}^{n_g}\omega_g\mathbf{B}_I^T\left(\mathbf{x}_{Qg}\right)\mathbf{C}\left(\mathbf{x}_{Qg};\mathbf{d}^i_{(j-1)}\right)\mathbf{B}_J\left(\mathbf{x}_{Qg}\right)\left|\mathbf{J}_{gc}\right| \tag{38}$$

where ω_g is the Gauss weighting factors for the gth Gauss point (g = 1,…,n_g) at $\mathbf{x}_{Qg}$ and $\mathbf{J}_{gc}$ is the Jacobian matrix for the area integration of the background cell c (c = 1,…,n_c), at which the Gauss point $\mathbf{x}_{Qg}$ is located.

4.2. On the solution of the nonlinear system of equations

The main numerical issue lies in the solution of a set of equations which are nonlinear because of the nonlinear behavior of, both, concrete and reinforcing steel. Moreover, it should be kept in mind that limit points can occur in the final load-displacement curves due to material nonlinearities such as work-softening or geometric nonlinearities. Although the maximum load capacity of a structure is the main interest in structural analysis and design, it may be important to investigate the entire response even beyond the occurrence of a limit point in order to identify failure modes as well as post-peak behavior.

Yang and Shieh [27] proposed the so-called Generalized Displacement Control Method (GDCM) with Generalized Stiffness Parameter (GSP). Cardoso and Fonseca [28] recently demonstrated that the GDCM is an arc-length method with orthogonal constraints. The method was originally applied to geometrically non-linear analyses and the results were found to be superior to most typical solvers. Recent results regarding the FE analysis of RC structures [29] and in-filled steel-concrete composite columns [30] demonstrated the validity of the GDCM in handling geometrically nonlinearities and softening-working materials such as concrete. In this work, the GDCM with GSP is used for nonlinear meshfree analyses, and the most important steps are described below.

4.3. Generalized displacement control method

A convenient decomposition for Eq. (34) is the following

$$\mathbf{K}^i_{(j-1)}\Delta\hat{\mathbf{d}}^i_j={}^{ext}\hat{\mathbf{f}} \tag{39}$$

$$\mathbf{K}^i_{(j-1)}\Delta\tilde{\mathbf{d}}^i_j=\mathbf{r}^i_{(j-1)} \tag{40}$$

where

$$\Delta\mathbf{d}^i_j=\Delta\lambda^i_j\Delta\hat{\mathbf{d}}^i_j+\Delta\tilde{\mathbf{d}}^i_j \tag{41}$$

Based on Eq. (41), the displacement increment vector $\Delta\mathbf{u}^i_j$ is determined by making use of the meshfree basis functions and enforcing the essential (displacement) boundary conditions. The total displacement vector of the structure at the end of the jth iteration $\mathbf{u}^i_j$ is computed as

$$\mathbf{u}^i_j = \mathbf{u}^i_{(j-1)} + \Delta\mathbf{u}^i_j \tag{42}$$

The total applied load vector at the jth iteration of the ith incremental step ${}^{ext}\mathbf{f}^i_j$ relates to the reference load vector ${}^{ext}\hat{\mathbf{f}}$ as follows

$${}^{ext}\mathbf{f}^i_j = {}^{ext}\mathbf{f}^i_{(j-1)} + \Delta\,{}^{ext}\mathbf{f}^i_j = {}^{ext}\mathbf{f}^i_{(j-1)} + \Delta\lambda^i_j\,{}^{ext}\hat{\mathbf{f}} \tag{43}$$

It is understood that the following initial conditions hold

$$\mathbf{K}^i_0 = \mathbf{K}^{(i-1)}_l,\quad {}^{ext}\mathbf{f}^i_0 = {}^{ext}\mathbf{f}^{(i-1)}_l,\quad \mathbf{u}^i_0 = \mathbf{u}^{(i-1)}_l \tag{44}$$

where l is the last iteration of the last incremental step.

The load increment parameter $\Delta\lambda^i_j$ is an unknown and is determined by imposing a constraint condition. For the first iterative step j = 1, the GSP is introduced. For any load increment i at j = 1, $GSP_1{}^i$ is defined as

$$GSP^i_1 = \begin{cases} 1 & if\ \ i=1 \\ \dfrac{\left(\Delta\hat{\mathbf{u}}^1_1\right)^T\left(\Delta\hat{\mathbf{u}}^1_1\right)}{\left(\Delta\hat{\mathbf{u}}^{(i-1)}_1\right)^T\left(\Delta\hat{\mathbf{u}}^i_1\right)} & if\ \ i\geq 2 \end{cases} \tag{45}$$

Therefore, for any load increment i at the first iterative step j = 1, $\Delta\lambda^i{}_1$ is determined based on Eq. (45)

$$\Delta\lambda^i_1 = \pm\Delta\lambda^1_1\sqrt{\left|GSP^i_1\right|} \tag{46}$$

where $\Delta\lambda^1{}_1$ is an initial value of the load increment parameter. The sign in Eq. (46) depends on the sign of the GSP. In fact, the GSP is negative only for the load step "immediately after" a limit point whereas it will always be positive for the other load steps. This is because the numerator is always positive, but the denominator could be negative if the two vectors have different directions. The GSP by itself is a useful indicator for changing the loading directions. Therefore, initially let $\Delta\lambda^i{}_1$ be of the same sign as $\Delta\lambda_1{}^{(i-1)}$: if $GSP^i{}_1$ is negative, then $\Delta\lambda^i{}_1$ is multiplied by –1 to reverse the direction of the loading.

For the iterative step $j\geq 2$, the load increment parameter $\Delta\lambda^i_j$ is calculated as

$$\Delta\lambda_j^i = -\frac{\left(\Delta\hat{\mathbf{u}}_1^{(i-1)}\right)^T\left(\Delta\tilde{\mathbf{u}}_j^i\right)}{\left(\Delta\hat{\mathbf{u}}_1^{(i-1)}\right)^T\left(\Delta\hat{\mathbf{u}}_j^i\right)} \tag{47}$$

Here, $\Delta\hat{\mathbf{u}}_1^{(i-1)}$ is the displacement increments generated by the reference load $\hat{\mathbf{p}}$ at the first iteration (j = 1) of the (i–1)th (previous) incremental step, and $\Delta\hat{\mathbf{u}}_j^i$ and $\Delta\tilde{\mathbf{u}}_j^i$ denote the displacement increments generated by the reference loads and unbalanced forces, respectively, at the jth iteration of the ith incremental step. Note that meshfree basis functions are required to calculate the displacement increments on solving the linear system of equations in Eq. (39) and Eq. (40). For the first increment i = 1, $\Delta\hat{\mathbf{u}}_1^0$ will be taken equal to $\Delta\hat{\mathbf{u}}_1^1$. A convergence criterion based on, both, the incremental displacements and the unbalanced force vector is used. The flowchart of the numerical method is shown in Fig 3.

4.4. Maximum-entropy basis functions

On denoting $\mathbf{x}_a$ (a = 1,…m) as the nodal coordinates, the displacement field in Eq. (29) can be rewritten as

$$\mathbf{u}^h(\mathbf{x}) = \sum_a^m \phi_a(\mathbf{x})\mathbf{d}_a \tag{48}$$

There are many choices to define meshfree basis functions, for example moving least squares (MLS) approximants, radial basis functions (RBF) and maximum-entropy (max-ent) approximants, to name a few. An overview about the construction of meshfree basis functions is presented in Ref. [31]. The principle of maximum entropy postulated by Jaynes [32] on the basis of the Shannon-entropy was recently exploited in order to construct meshfree basis functions. Shannon-entropy based construction of max-ent basis functions on polygons was proposed by Sukumar [33], and a modified entropy functional was exploited by Arroyo and Ortiz [34]. Introducing the notion of prior weight function, Sukumar and Wright [31] obtained the max-ent basis functions which generalizes the entropy functional considered in Ref. [34]. The first application of the maximum entropy meshfree (MEM) method in the field of structural engineering is presented in Ref. [2].

Max-ent basis functions are promising because they are a convex combination and possess a variation diminishing property as well as a weak Kronecker-delta property on the boundary [34]. An implication of the weak Kronecker-delta property is that essential boundary conditions can be imposed as in FE methods. This is a noteworthy advantage with respect to most meshfree approximants (i.e., MLS), which require special techniques to enforce essential boundary conditions. Max-ent approximants also allow to blend FE and meshfree basis functions in a

seamless fashion. For completeness, a short review about the derivation of max-ent basis functions follows.

The max-ent basis functions ϕ_a (a = 1,…m) are obtained by solving the following optimization problem [31]

$$\max_{\phi\in\mathbb{R}_+^m}\left\{-\sum_a^m \phi_a(\mathbf{x})\ln\left(\frac{\phi_a(\mathbf{x})}{w_a(\mathbf{x})}\right)\right\} \tag{49}$$

subjected to

$$\sum_a^m \phi_a(\mathbf{x}) = 1 \tag{50}$$

$$\sum_a^m \phi_a(\mathbf{x})\boldsymbol{\xi}_a(\mathbf{x}) = \mathbf{0} \tag{51}$$

where $\boldsymbol{\xi}_a=\mathbf{x}_a-\mathbf{x}$ are shifted nodal coordinates and $w_a(\mathbf{x})$ is the prior weight function (initial guess for ϕ_a). The first constraint in Eq. (50) imposes the partition of unity property in order to represent rigid body translations (zeroth-order reproducibility). Basis functions that satisfy the set of constrains in Eq. (51) can reproduce a constant strain field exactly (first-order reproducibility). Once the variational problem in Eqs. (49)-(51) is solved by means of the Lagrange multipliers technique, the following result for the max-ent basis functions is obtained [31]:

$$\phi_a(\mathbf{x}) = \frac{Z_a(\mathbf{x};\boldsymbol{\eta}^*)}{Z(\mathbf{x};\boldsymbol{\eta}^*)} \tag{52}$$

where

$$Z_a(\mathbf{x};\boldsymbol{\eta}^*) = w_a(\mathbf{x})\exp\{-\boldsymbol{\eta}^*\cdot\boldsymbol{\xi}_a\} \tag{53}$$

and

$$Z(\mathbf{x};\boldsymbol{\eta}^*) = \sum_b^m Z_b(\mathbf{x};\boldsymbol{\eta}^*) \tag{54}$$

is the so-called partition function. The Lagrange multipliers vector $\boldsymbol{\eta}^*$ is obtained by solving the dual optimization problem

$$\boldsymbol{\eta}^* = \arg\min_{\boldsymbol{\eta}\in\mathbb{R}^2}\{\ln Z(\mathbf{x};\boldsymbol{\eta})\} \tag{55}$$

that leads to the following system of nonlinear equations:

$$\nabla_{\boldsymbol{\eta}} \ln Z(\boldsymbol{\eta}) = -\sum_{a}^{m} \phi_a(\mathbf{x}) \boldsymbol{\xi}_a(\mathbf{x}) = \mathbf{0} \tag{56}$$

Standard Newton-based solvers can be used for Eq. (56), and the convergence is typically very fast. Once the converged Lagrange multipliers $\boldsymbol{\eta}^*$ are calculated, the gradient of the max-ent basis functions are evaluated as follows:

$$\nabla \phi_a = \phi_a \left[\boldsymbol{\xi}_a \cdot \left(\mathbf{H}^{-1} - \mathbf{H}^{-1} \cdot \mathbf{A} \right) + \frac{\nabla w_a}{w_a} - \sum_{b}^{m} \phi_b \frac{\nabla w_b}{w_b} \right] \tag{57}$$

where

$$\mathbf{A} = \sum_{b}^{m} \phi_b \boldsymbol{\xi}_b \otimes \frac{\nabla w_b}{w_b} \tag{58}$$

and $\mathbf{H}$ is the Hessian matrix

$$\mathbf{H} = \nabla_{\boldsymbol{\eta}} \nabla_{\boldsymbol{\eta}} \ln Z(\boldsymbol{\eta}) = \sum_{b}^{m} \phi_b \boldsymbol{\xi}_b \otimes \boldsymbol{\xi}_b \tag{59}$$

As the prior weight function, quartic polynomials are used in this study:

$$w_a(\mathbf{x}) = \begin{cases} 1 - 6q^2 + 8q^3 - 3q^4 & 0 \le q \le 1 \\ 0 & q > 1 \end{cases} \tag{60}$$

where $q = \|\mathbf{x}_a - \mathbf{x}\| / r_a$ and r_a is the radius of the basis function support at node *a*.

5. Validation

5.1. Analysis of RC shear walls

The nonlinear response of a variety of two-dimensional RC structural elements under plane stress – e.g., beams and shear walls – may be analyzed by means of the MEM method.

Current approaches in modeling RC shear walls can be classified as follows [25]: beam-column type models in which flexure is the dominant mode of response, multi-spring based macro-models and FE based microscopic models. In this study, the proposed MEM method is adopted as an alternative technique for the analysis of RC shear walls.

5.2. Comparison with experimental data

To verify the reliability of the presented meshfree method, the large scale RC shear walls tested by Lefas and co-workers [35] are investigated and numerical simulations are compared to experimental

results. In their work, Lefas and co-workers considered two types of RC shear walls having constant thickness. Type I walls were 750 mm high, 750 mm wide and 70 mm thick. Type II walls were 1300 mm high, 650 mm wide and 65 mm thick. Specimens consisted of two lateral ribs, a top slab and a bottom base block. The vertical and horizontal reinforcement comprised high-tensile deformed steel bars of 8 and 6.25 mm diameter, respectively. Additional horizontal reinforcement in the form of stirrups confined the wall edges. Mild steel bars of 4 mm diameter were used for this purpose. Lateral ribs with confinement reinforcement provide two concealed columns with rectangular shape at each edge of the shear wall. The RC shear wall specimens were subjected to the combined action of a distributed vertical load and a horizontal load at the upper beam (load-controlled testing).

In this study, specimens SW14 and SW15 are investigated for Type I RC shear walls whereas specimens SW21 and SW22 are considered for Type II RC shear walls. Input data on the imposed load, concrete and reinforcing steel are listed in Table 1 and 2. The top slab served to distribute both the horizontal and the vertical loads. The base block, clamped to the laboratory floor, simulated a rigid foundation. Having this in mind, the base block is replaced with a set of deformation constraints and the vertical and horizontal load are uniformly distributed over the wall width. Starting from the input data listed in Table 1 and 2, the remaining mechanical data are determined as follows. Values for the concrete compressive strength f_c' are specified as 85% of the cube compressive strength values. For concrete in tension, E_{ct0} is calculated on assuming $\varepsilon_{ct} = 0.00008$ [26] and $f_{ct} = 0.33(f_c')^{0.5}$ [16]. The mode-*I* fracture energy of concrete is calculated based on the maximum aggregate size $d_{\max}$ of 10 mm. The initial (elastic) modulus for steel is 200,000 MPa. A small number of preliminary runs were performed to investigate β, ν and μ values in the ranges [2.00,5.00], [0.15,0.20] and [0.10,1.00], respectively.

The GDCM is performed by assuming $\Delta\lambda^1_1 = 0.005$ and the tolerance for convergence was set to 10^{-5}. A regular nodal arrangement is used at first. The adopted nodal spacing is 75 mm × 75 mm for specimens SW14 and SW15 and 65 mm × 65 mm for specimens SW21 and SW22.

Assuming this set of input data, the final load-displacement curves in Fig. 4 are obtained. Numerical results appear to be in satisfactory agreement with the experimental observations. Obviously, some of the discrepancies may be attributed to the unavoidable uncertainties and approximations in, both, models and parameters, which are not insignificant in RC modeling. However, another factor may also be the source of disagreement between numerical and experimental results. It is observed that numerical results for the initial lateral stiffness are higher than those observed experimentally. This may be due to the foundation flexibility of the RC shear wall which has not been considered in this analysis. In this simulation the base block was replaced with a set of rigid constraints, thus

overestimating the shear wall foundation stiffness. The overestimation is less severe for walls with imposed axial loads. The presence of axial loading more closely approximates the rigid constraints assumed at the base block. Therefore, under zero or very low axial loads, replacing the base block with a set of rigid constraints is less consistent with the experiment. Following this argument, one may justify why the agreement with experimental data is better for SW22 than for SW15. In fact, the shear wall flexibility increases considerably with respect to the base block as the shear wall height doubles, and then replacing the base block with rigid constraints is more appropriate in SW22 than in SW15. However, the foundation flexibility should have no significant effects on the load capacity as well as on its post-peak behavior because the failure mechanism essentially involves the behavior of the shear wall.

About the numerical procedure, it is found that 2 iterations are needed for each increment when considering SW14 and SW21. A larger number of iterations (3 or 4) are needed to achieve the equilibrium at each increment for specimens SW15 and SW22.

5.3. Comparison with FE methods

Experimental data from Ref. [35] were also used by many other authors to validate their FE based analyses [16,24,36,37]. Likewise, the main features of the load-displacement curves obtained by the meshfree method presented in this paper are compared to FE simulations. A comparison between the obtained load-displacement curves and those presented in Ref. [36] is shown in Fig. 4. Kwan and He [36] adopted a smeared crack approach in concrete modeling as well as considering cracked concrete to be an orthotropic material, but there is no information on the reinforcing steel model in their work. They also considered the confinement effect in modeling the compressive concrete strength at the lateral ribs and a standard displacement control method was used to track the post-peak behavior of the shear walls. Accounting for the differences in RC modeling, the presented MEM method and the FE analysis by Kwan and He [36] are in satisfactory agreement.

The meshfree results are compared to that in Ref. [37]. Park and Kim [37] presented a microplane based FE analysis of planar RC structures, and validated their method using load-displacement curves also considered in the present study, that is the experimental responses for SW21 and SW22 specimens. A qualitative comparison between the obtained results in Fig. 4 and those presented in Ref. [37] confirms the validity of the presented MEM method. Specifically, the illustrated meshfree method provides a better estimation of the load capacity for the SW21 specimen, along with a more consistent prediction of the corresponding displacement. The meshfree-based estimation of the ultimate displacement for this shear wall is in very good agreement with the FE results of Park and Kim [37]. A general good agreement is observed in the simulation of the SW22 specimen, even if

the meshfree-based prediction of the ultimate displacement seems to be lower than that in Ref. [37].

5.4. Effects of different nodal arrangements

The effects of different nodal arrangements on the load-displacement response are shown in Fig. 5 for specimen SW22. The irregular nodal arrangement was obtained by perturbing the regular one, and the magnitude of the perturbation was 3%. Further strategies may be implemented to improve the numerical method as well as the reliability of the final results. For instance, the use of nodal integration techniques along with appropriate stabilization methods can be exploited to achieve a completely meshfree method. Non-local approaches can also be used to improve the objectivity of smeared crack models based results.

5.5. Stress-strain prediction

Experimental data of the shear walls A2 and A3 tested by Pang and Hsu [38] are finally taken into account. The panels were 55 in. high, 55 in. wide and 7 in. thick. The maximum compressive cylinder concrete strength was 5.98 ksi and 6.04 ksi for A2 and A3, respectively. The corresponding strain values were 0.00210 and 0.00194. Reinforcement was arranged at 45 deg with respect to the x axis. The steel reinforcing ratio is 0.01193 for A2 and 0.01789 for A3, with equal amounts in the two perpendicular directions. The corresponding yield strengths were 67.10 ksi and 64.75 ksi, respectively. The principal compressive and tensile stresses of equal magnitude were applied in the vertical and horizontal direction, respectively. Such a proportional static loading leads to a shear-based stress condition in the 45° direction. The applied shear stress and the shear strain were monitored along the system reference of the reinforcing bars.

The results in Fig. 6 show a good agreement between experimental data and numerical simulations. The yielding point of the reinforcing steel is evident and well predicted. The maximum applied shear stress was reached when the concrete began crushing. From this point on, the curves went into the descending branches that are satisfactorily simulated. The meshfree-based simulation of the A3 specimen is in good agreement with the FE analysis of Wang and Hsu [38].

6. Conclusions

This study presented a maximum-entropy meshfree method for material nonlinear analysis of two-dimensional RC structures subjected to proportional monotonic static loading. Concrete and reinforcing steel modeling were first discussed, and the generalized displacement control method was implemented in order to solve the final nonlinear system of equations. As a validation study, RC shear walls were considered, and comparison of numerical simulations with experimental data

as well as finite element (FE) analysis demonstrated the suitability of the presented maximum-entropy meshfree method.

However, meshfree methods are not exempt from drawbacks, i.e. a larger computational effort than FE approaches. A competitive computational framework can be formulated in such a way that FE methods are used where meshless approaches are not an efficient option whereas meshfree methods are adopted where FE based techniques are known to be problematic. Moving from this consideration, next studies will address a blended FE-meshfree analysis of RC structures subjected to cyclic loadings. In doing so, the use of max-ent approximants is particularly suitable because it provides a seamless bridge between FE and meshfree basis functions.

References

[1] Yaw L.L., Kunnath S.K., Sukumar N. Meshfree method for inelastic frame analysis. Journal of Structural Engineering, 135(6), 676-684, 2009

[2] Yaw L.L., Sukumar N., Kunnath S.K. Meshfree co-rotational formulation for two-dimensional continua. International Journal for Numerical Methods in Engineering, 79(8), 979-1003, 2009

[3] Rabczuk T., Zi G., Bordas S., Nguyen-Xuan H. A geometrically non-linear three-dimensional cohesive crack method for reinforced concrete structures. Engineering Fracture Mechanics, 75(16), 4740-4758, 2008

[4] Rabczuk T., Eibl J. Numerical analysis of prestressed concrete beams using a coupled element free Galerkin/finite element approach. International Journal of Solids and Structures, 41(3-4), 1061-1080, 2004

[5] He W., Wu Y.F., Liew K.M. A fracture energy based constitutive model for the analysis of reinforced concrete structures under cyclic loading. Computer Methods in Applied Mechanics and Engineering, 197(51-52), 4745-4762, 2008

[6] Yang Z.J., Chen J. Finite element modelling of multiple cohesive discrete crack propagation in reinforced concrete beams. Engineering Fracture Mechanics, 72(14), 2280-2297, 2005

[7] Pietruszczak S., Stolle D.F.E. Deformation of strain softening materials. Part I: Objectivity of finite element solutions based on conventional strain softening formulations. Computers and Geotechnics, 1(2), 99-115, 1985

[8] Mo Y.L., Zhong J., Hsu T.T.C. Seismic simulation of RC wall-type structures. Engineering Structures, 30(11), 3167-3175, 2008

[9] Kwak H.G., Filippou F.C. Finite element analysis of reinforced concrete structures under monotonic loads. Technical report no. UCB/SEMM-90/14, University of California Barkeley, 1990

[10] Bažant Z.P. Oh B.H. Crack band theory for fracture of concrete. Materiaux et Constructions, 16(93), 155-177, 1983

[11] Vecchio F.J., Collins M.P. Modified compression-field theory for reinforced concrete elements subjected to shear. ACI Journal, 83(2), 219-31, 1986

[12] Kabeyasawa T., Milev J.I. Modeling of reinforced concrete shear walls under varying axial load. Transactions of the 14th International Conference on Structural Mechanics in Reactor Technology (SMiRT 14), Lyon, France, August 17-22, 1997

[13] Darwin D., Pecknold D.A. Inelastic model for cyclic biaxial loading of reinforced concrete. Technical report, Structural Research Series 409, College of Engineering. University of Illinois at Urbana-Champaign, 1974

[14] Hu H.T., Schnobrich W.C. Nonlinear finite element analysis of reinforced concrete plates and shells under monotonic loading. Computers and Structures, 38(516), 631-651, 1991

[15] Hoshikuma J., Kawashima K., Nagaya K., Taylor A.W. Stress-strain model for confined reinforced concrete in bridge piers. Journal of Structural Engineering, 123(5), 624-633, 1997

[16] Vecchio F.J. Finite element modeling of concrete expansion and confinement. Journal of Structural Engineering, 118(9), 2390-2406, 1992

[17] Zhu R.R.H., Hsu T.T.C. Poisson effect of reinforced concrete membrane elements. ACI Structural Journal, 99(5), 631-640, 2002

[18] Noh S.Y., Krätzig W.B., Meskouris K. Numerical simulation of serviceability, damage evolution and failure of reinforced concrete shells. Computers and Structures, 81(8-11), 843-857, 2003

[19] Krätzig W., Pölling R. An elasto-plastic damage model for reinforced concrete with minimum number of material parameters. Computers and Structures, 82(15-16), 1201-1215, 2004

[20] CEB-FIP model code (design code), Comité Euro-International du Béton. Thomas Telford Ltd, 1993

[21] Popovics S. A numerical approach to the complete stress-strain curve of concrete. Cement and Concrete Research, 3(5), 583-599, 1973

[22] Zhu R. H., Hsu T. T. C., Lee J. Y. Rational shear modulus for smeared crack analysis of reinforced concrete. ACI Structural Journal, 98(4), 443-550, 2001

[23] He W., Wu Y.F., Liew K.M., Wu Z. A 2D total strain based constitutive model for predicting the behaviors of concrete structures. International Journal of Engineering Science, 44(18-19), 1280-1303, 2006

[24] Kwak H.G., Kim D.Y. Material nonlinear analysis of RC shear walls subject to monotonic loadings. Engineering Structures, 26(11), 1517-1533, 2004

[25] Bao Y., Kunnath S.K. Simplified progressive collapse simulation of RC frame-wall structures. Engineering Structures, 32(10), 3153-3162, 2010

[26] Mansour M., Lee J.-Y., Hsu T.T.C. Cyclic stress-strain curves of concrete and steel bars in membrane elements. Journal of Structural Engineering, 127(12), 1402-1411, 2001

[27] Yang Y.-B., Shieh M.-S. Solution method for nonlinear problems with multiple critical points. AIAA Journal, 28(2), 2110-2116, 1990

[28] Cardoso E.L., Fonseca J.S.O The GDC method as an orthogonal arc-length method. Communications in Numerical Methods in Engineering, 23(4), 263-271, 2007

[29] Gomes H.M.M., Awruch A.M. Some aspects on three-dimensional numerical modeling of reinforced concrete structures using the finite element method. Advances in Engineering Software, 32(1), 257-277, 2001

[30] Lakshmi B., Shanmugam N.E. Nonlinear analysis of in-filled steel-concrete composite columns. Journal of Structural Engineering, 128(7), 922-933, 2002

[31] Sukumar N., Wright R.W. Overview and construction of meshfree basis functions: From moving least squares to entropy approximants. International Journal for Numerical Methods in Engineering, 70(2), 181-205, 2007

[32] Jaynes E.T. Information theory and statistical mechanics. Physical Review. 106(4), 620-630, 1957

[33] Sukumar N. Construction of polygonal interpolants: a maximum entropy approach, International Journal for Numerical Methods in Engineering, 61(12), 2159-2181, 2004

[34] Arroyo M., Ortiz M. Local maximum-entropy approximation schemes: a seamless bridge between finite elements and meshfree methods. International Journal for Numerical Methods in Engineering, 65(13), 2167-2202, 2006

[35] Lefas I.D., Kotsovos M.D., Ambraseys N.N. Behavior of reinforced concrete structural walls: strength, deformation characteristics, and failure mechanism. ACI Structural Journal, 87(1), 23-31, 1990

[36] Kwan A.K.H., He X.G. Finite element analysis of effect of concrete confinement on behavior of shear walls. Computers and Structures 79(19), 1799-1810, 2001

[37] Park H., Kim H. Microplane model for reinforced-concrete planar members in tension-compression. Journal of Structural Engineering, 129(3), 337-345, 2003

[38] Pang X.B., Hsu T.T.C. Behavior of reinforced concrete membrane elements in shear. ACI Structural Journal, 92(6), 665-677, 1995

[39] Wang T., Hsu T.T.C. Nonlinear finite element analysis of concrete structures using new constitutive models, Computers and Structures, 79(32), 2781-2791, 2001

List of figures

Fig. 1. Concrete modeling (not to scale)

Fig. 2. Modeling of steel reinforcement (not to scale)

Fig. 3. Generalized displacement control method for meshfree nonlinear analyses

Fig. 4. Comparison between experimental data, finite element analysis and maximum-entropy meshfree method

Fig. 5. Effects of different nodal arrangements

Fig. 6. Comparison between shear stress-shear strain experimental curves and maximum-entropy meshfree method

List of tables

Table 1. Load and concrete data from Ref. [35]

Table 2. Reinforcing steel data from Ref. [35]

Shear wall identification		Vertical load [kN]	Cubic uniaxial concrete strength [MPa]
Type	Specimen		
I	SW14	0	42.1
	SW15	185	43.3
II	SW21	0	42.8
	SW22	182	50.6

Table 1

Type	Yield strength [MPa]	Ultimate strength [MPa]
8 mm high-tensile bar	470	565
6.25 mm high-tensile bar	520	610
4 mm mild-steel bar	420	490

Table 2

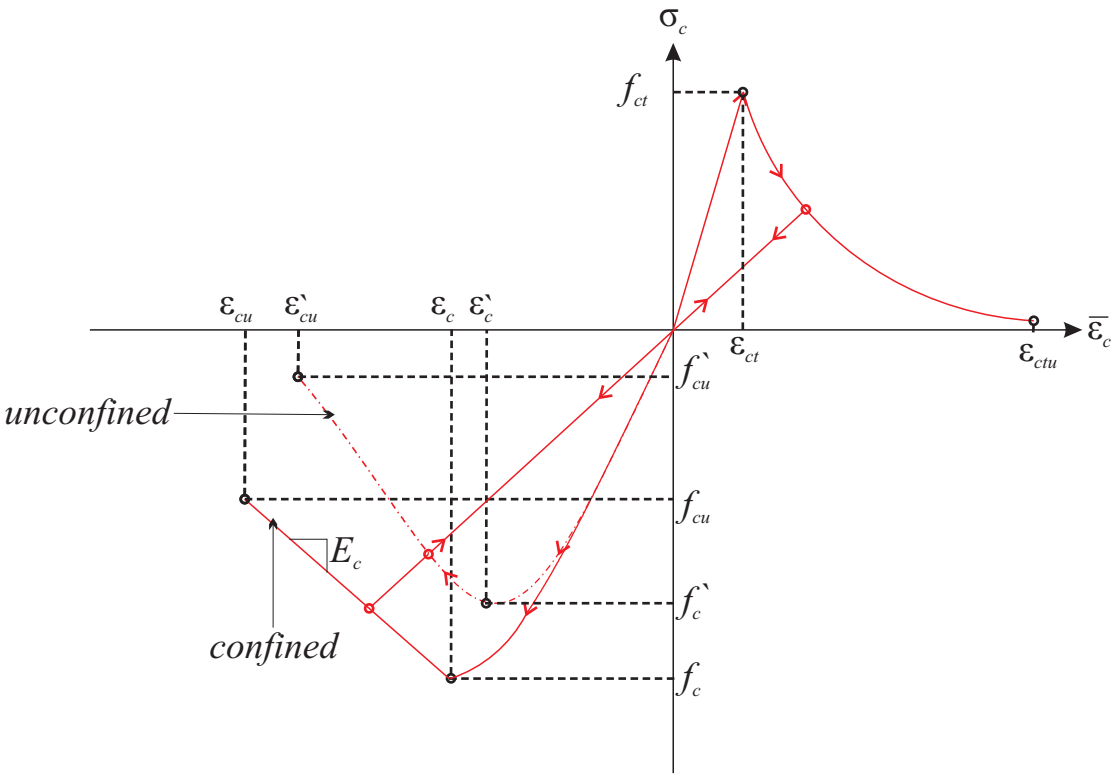
σc
fct
εcu
ε`cu
εc
ε`c
εct
εctu
ε̄c
f`cu
unconfined
fcu
Ec
f`c
confined
fc

Fig. 1

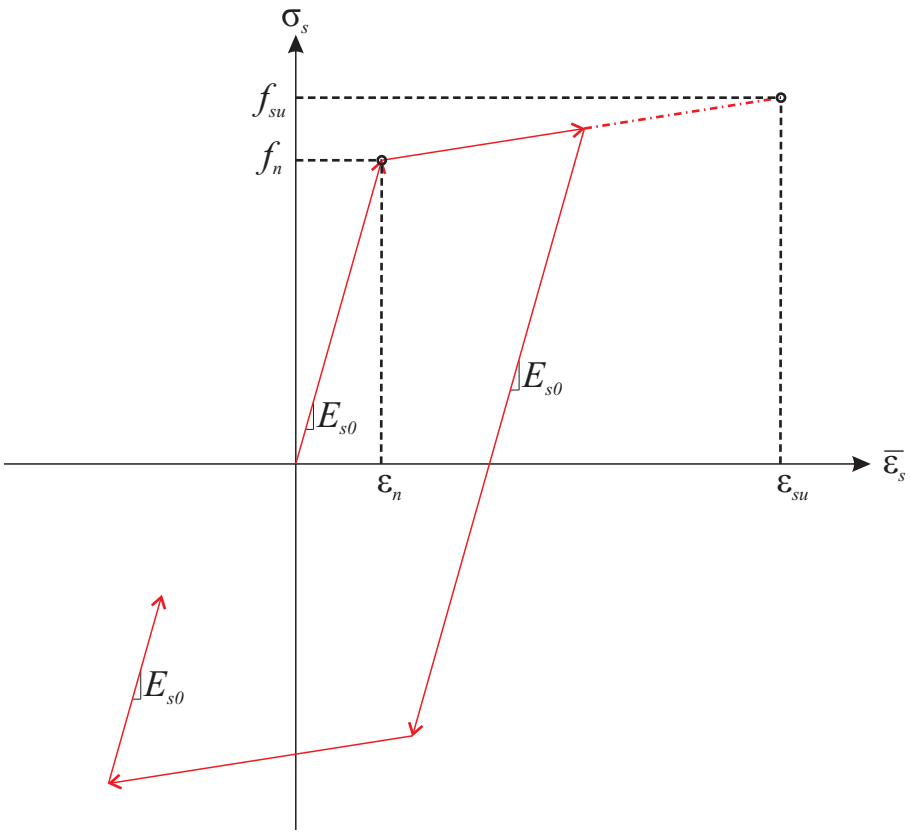

Fig. 2

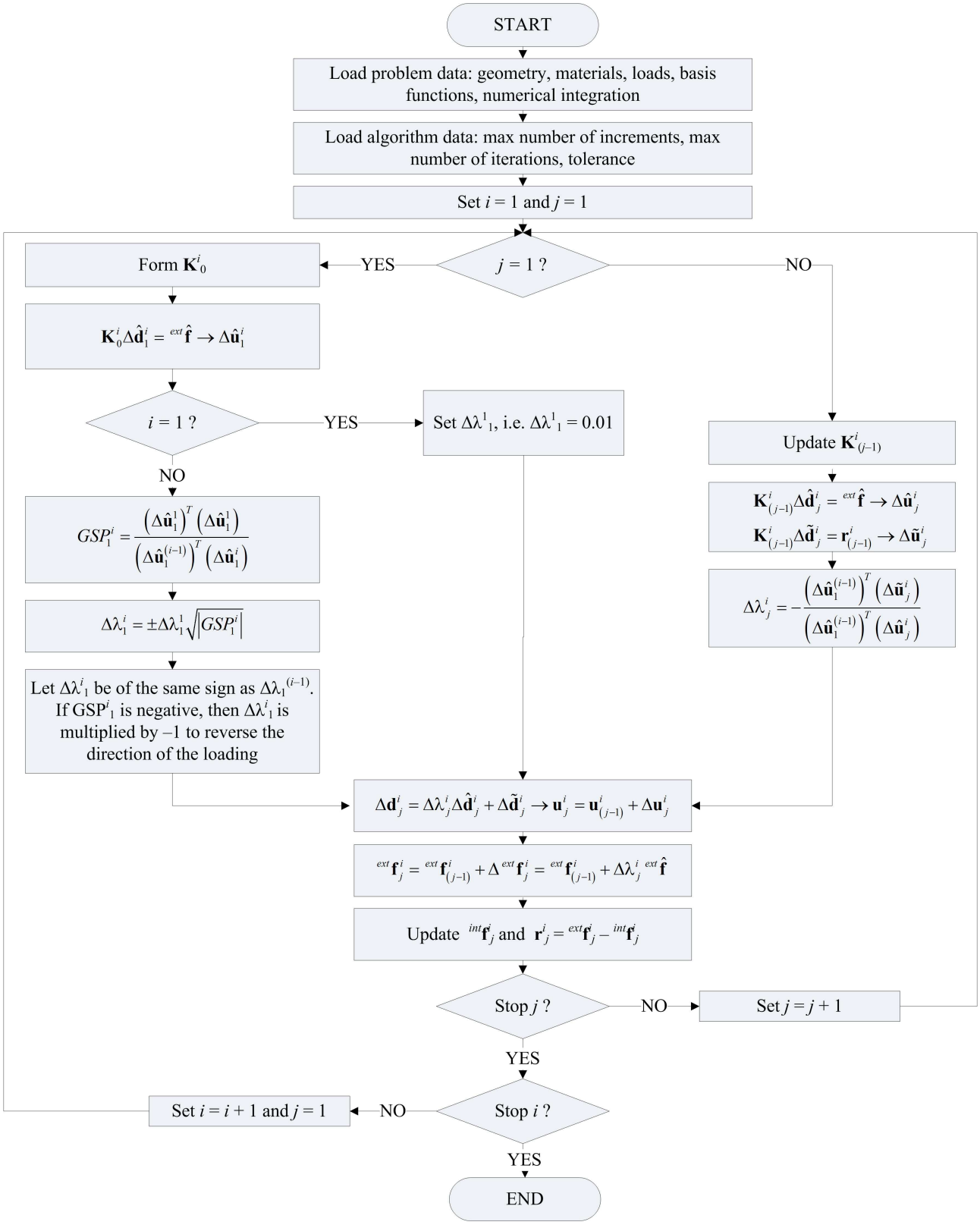
START
Load problem data: geometry, materials, loads, basis functions, numerical integration
Load algorithm data: max number of increments, max number of iterations, tolerance
Set $i = 1$ and $j = 1$
$j = 1$?
YES
NO
Form $\mathbf{K}^i_0$
$\mathbf{K}^i_0 \Delta\hat{\mathbf{d}}^i_1 = {}^{ext}\hat{\mathbf{f}} \rightarrow \Delta\hat{\mathbf{u}}^i_1$
$i = 1$?
YES
Set $\Delta\lambda^1_1$, i.e. $\Delta\lambda^1_1 = 0.01$
NO
$GSP^i_1 = \dfrac{\left(\Delta\hat{\mathbf{u}}^1_1\right)^T \left(\Delta\hat{\mathbf{u}}^1_1\right)}{\left(\Delta\hat{\mathbf{u}}^{(i-1)}_1\right)^T \left(\Delta\hat{\mathbf{u}}^i_1\right)}$
$\Delta\lambda^i_1 = \pm\Delta\lambda^1_1 \sqrt{\left|GSP^i_1\right|}$
Let $\Delta\lambda^i_1$ be of the same sign as $\Delta\lambda_1{}^{(i-1)}$. If GSP^i_1 is negative, then $\Delta\lambda^i_1$ is multiplied by –1 to reverse the direction of the loading
Update $\mathbf{K}^i_{(j-1)}$
$\mathbf{K}^i_{(j-1)} \Delta\hat{\mathbf{d}}^i_j = {}^{ext}\hat{\mathbf{f}} \rightarrow \Delta\hat{\mathbf{u}}^i_j$
$\mathbf{K}^i_{(j-1)} \Delta\tilde{\mathbf{d}}^i_j = \mathbf{r}^i_{(j-1)} \rightarrow \Delta\tilde{\mathbf{u}}^i_j$
$\Delta\lambda^i_j = -\dfrac{\left(\Delta\hat{\mathbf{u}}^{(i-1)}_1\right)^T \left(\Delta\tilde{\mathbf{u}}^i_j\right)}{\left(\Delta\hat{\mathbf{u}}^{(i-1)}_1\right)^T \left(\Delta\hat{\mathbf{u}}^i_j\right)}$
$\Delta\mathbf{d}^i_j = \Delta\lambda^i_j \Delta\hat{\mathbf{d}}^i_j + \Delta\tilde{\mathbf{d}}^i_j \rightarrow \mathbf{u}^i_j = \mathbf{u}^i_{(j-1)} + \Delta\mathbf{u}^i_j$
${}^{ext}\mathbf{f}^i_j = {}^{ext}\mathbf{f}^i_{(j-1)} + \Delta\,{}^{ext}\mathbf{f}^i_j = {}^{ext}\mathbf{f}^i_{(j-1)} + \Delta\lambda^i_j\,{}^{ext}\hat{\mathbf{f}}$
Update ${}^{int}\mathbf{f}^i_j$ and $\mathbf{r}^i_j = {}^{ext}\mathbf{f}^i_j - {}^{int}\mathbf{f}^i_j$
Stop j ?
NO
Set $j = j + 1$
YES
Stop i ?
NO
Set $i = i + 1$ and $j = 1$
YES
END

Fig. 3

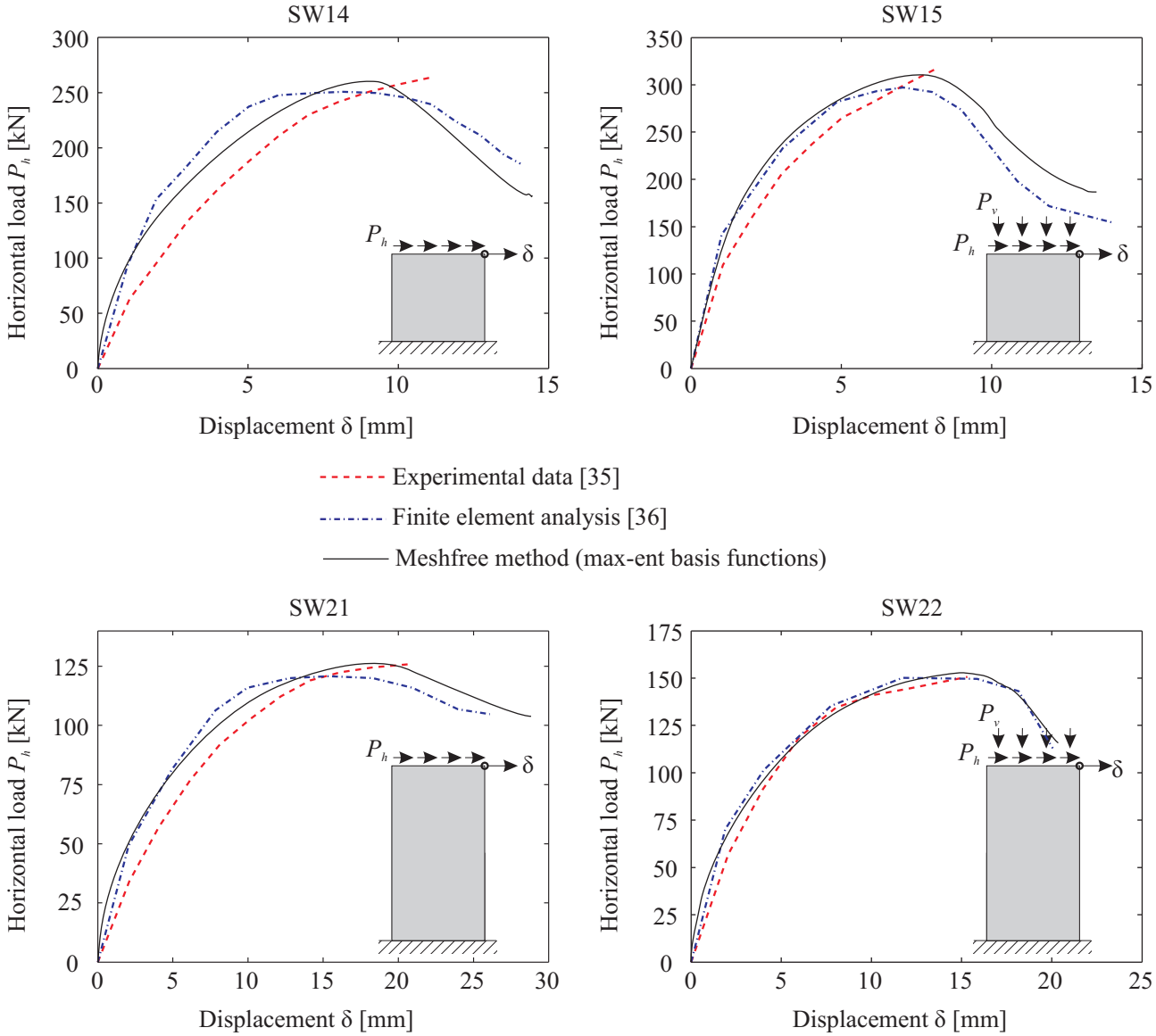
SW14
SW15
SW21
SW22
Horizontal load P_h [kN]
Displacement δ [mm]
P_h
P_v
δ
Experimental data [35]
Finite element analysis [36]
Meshfree method (max-ent basis functions)

Fig. 4

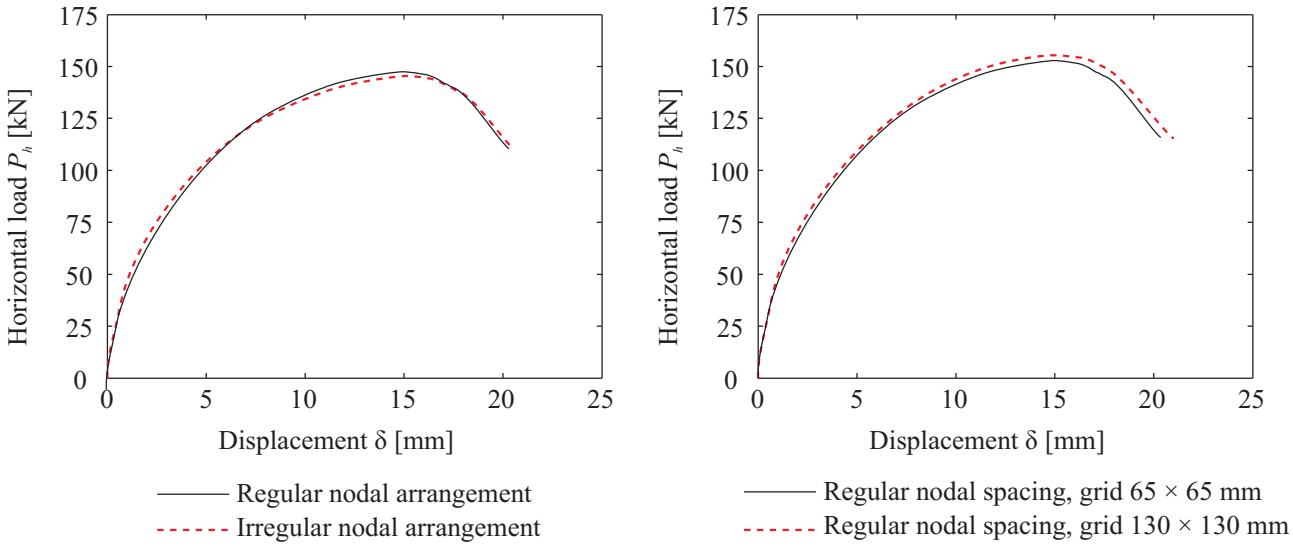
Horizontal load P_h [kN]
175
150
125
100
75
50
25
0
0
5
10
15
20
25
Displacement δ [mm]
Regular nodal arrangement
Irregular nodal arrangement
Horizontal load P_h [kN]
175
150
125
100
75
50
25
0
0
5
10
15
20
25
Displacement δ [mm]
Regular nodal spacing, grid 65 × 65 mm
Regular nodal spacing, grid 130 × 130 mm

Fig. 5

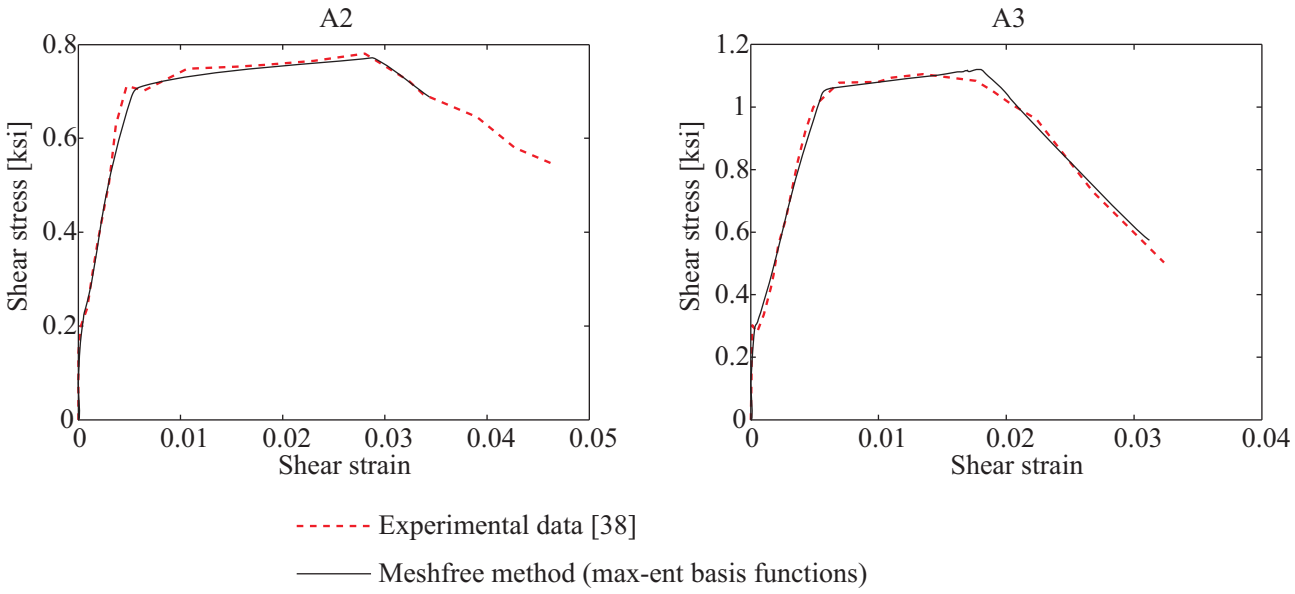
A2
A3
Shear stress [ksi]
Shear strain
0
0.01
0.02
0.03
0.04
0.05
0.2
0.4
0.6
0.8
1
1.2
Experimental data [38]
Meshfree method (max-ent basis functions)

Fig. 6